Millimeter Wave Image Super Resolution Using Multichannel Depth Convolution Neural Network

Ruyue Peng¹, Jianfei Chen¹, *, Zhao Liu², and Zhimin Guo¹

Abstract—Benefit from the high resolution, penetrating and all-weather advantages of millimeter-wave (MMW) imaging, MMW imaging plays an important role in remote sensing, security inspection, navigation, etc. Among the MMW imaging systems, synthetic aperture imaging radiometer (SAIR) utilizes aperture synthetic technology to achieve higher imaging resolution, but the perception information is insufficient, resulting in poor image quality. To improve the image quality of passive SAIR MMW images effectively, we propose a novel multichannel depth convolutional neural network (MDCNN) in this paper. Aiming at the characteristics of original MMW images with more noise in low-frequency information and fewer features in high-frequency information, wavelet transform is incorporated into the MDCNN to obtain the high- and low-frequency components first. Then, dense residual block and skip connection technology are adopted to denoise and enhance target information in the four independent channels respectively. Finally, high-quality MMW images are synthesized by inverse wavelet transform. The simulation results show that the reconstructed images of MDCNN have better image quality (such as image contour and texture details) than other deep learning-based methods.

1. INTRODUCTION

Millimeter wave (MMW) is located in the overlapping range of far-infrared wave and microwave, which has better penetration ability than far-infrared wave. Compared with microwave, its imaging resolution is higher. In addition, MMW is not affected by light and can be monitored all day. Based on these advantages, MMW imaging plays an important role in remote sensing, security inspection, navigation, etc. [1]. Among many MMW imaging systems, synthetic aperture imaging radiometer (SAIR) uses aperture synthesis technology to realize MMW imaging of super large aperture antenna [2]. Compared with traditional imaging techniques, SAIR has higher spatial resolution and better real-time performance. However, due to the weak target radiation signal and the limitation of a large aperture antenna array composed of small aperture antennas [3], some effective MMW information is difficult to be received, which ultimately leads to poor image quality generated by SAIR. Moreover, coupled with the influence of spherical wave and observation noise, near-field SAIR MMW image quality is worse, which is difficult to meet the subsequent image recognition and classification in specific fields. Therefore, it is necessary to enhance the SAIR MMW image.

At present, there are two research focuses for SAIR MMW image enhancement. One is to improve the imaging inversion accuracy based on imaging principle, and the other is to improve image quality based on image features. The imaging inversion accuracy can be improved by improving the accuracy of imaging models and imaging inversion processes, such as MFFT and G-matrix methods. By adding phase compensation terms, MFFT effectively improves the imaging inversion accuracy, and thus obtains

more accurate MMW images, especially in near-field conditions. Benefiting from the more accurate G-matrix model and numerical inversion process, the G-matrix-based inversion can obtain more accurate MMW images than MFFT [4]. However, due to the limitation of the antenna, observation noise, and errors in mathematical modeling and numerical inversion process, there is still a big gap between the SAIR MMW image obtained by the above inversion methods and the real image. Therefore, it is necessary to enhance the image quality based on the prior information of the image. Relevant literature has proved that the super-resolution (SR) method has more advantages in improving image quality based on image features, so SR method is used to enhance MMW images in this paper. Image SR aims to reconstruct a high-resolution (HR) image from its degraded low resolution (LR) [5], which can identify the effective information of scene objects and enhance the intelligibility of images. Plenty of image SR algorithms have been proposed, including interpolation-based [6], reconstruction-based, and learning-based methods. Among them, due to the self-iteration and optimization mechanism of deep learning, the method based on deep learning has more advantages in improving image quality. In 2014, Dong et al. firstly proposed a convolutional neural network for SR of optical images, named Super-Resolution Convolutional Neural Network (SRCNN), which achieved significant improvement over conventional methods and proved the superiority of deep learning technology in the field of image SR reconstruction [7]. Then, in order to improve the operation speed, Fast SRCNN (FSRCNN) with deconvolution layer was proposed [8]. The deconvolution layer simplifies the up sampling operation and reduces the convolution layer to reduce the number of parameters. Since the texture details of the image mainly exist in the high-frequency in formation part, a targeted residual network structure, VDSR [9], was proposed to effectively improve the texture details and achieved high-quality SR results. VDSR also showed that skip connection could reduce the amount of network data and the low training efficiency caused by network deepening. On this basis, for realizing the goal of further improving SR quality without reducing training efficiency, Enhanced Deep Super-Resolution Network (EDSR) [10] optimized the residual structure by reducing unnecessary Batch Normalization (BN) layers and increased the number of residual blocks to deepen the network. Furthermore, Residual Dense Network (RDN) model was proposed by combining residual network structure with dense connection network structure to deepen the network again and obtain better SR results [11]. The dense connection between layers and the residual learning method were used to fully mine the local feature information of the image and learn and store the feature information extracted separately.

The above SR methods are all aimed at optical images which have richer texture information, so the targeted residual block can achieve a better SR effect. However, for MMW images with less texture details, compared with enhancing texture information, focusing on the contour information is the key to MMW images SR research. Because of few studies working on the image contour information, considering that terahertz images have similar characteristics to MMW images, an SR algorithm named THZ containing residual blocks and skip connections is proposed for terahertz images and has achieved good results [12]. Compared with terahertz images, MMW images have limited high-frequency information, so the low-frequency contour information is more important for MMW images, which needs more targeted image enhancement processing. Therefore, this paper proposes a multichannel depth convolutional neural network (MDCNN) to achieve high-precision MMW images SR reconstruction. In MDCNN, the wavelet transform is used to divide the image into four components firstly, and the corresponding channel network structure is constructed according to the characteristics of each component. The SR MMW images are reconstructed from the results of four channels by inverse wavelet transform. Finally, the experimental results show that the method we proposed has more advantages in reconstruction quality than other image SR methods.

2. DESCRIPTION OF MDCNN

Due to the characteristics of SAIR MMW image, MDCNN using depth learning is proposed to realize higher-precision MMW image. The structure diagram of MDCNN is shown in Fig. 1. Considering the lack of large MMW images data set, we use SAIR simulator to generate many LR MMW images as shown in Fig. 1(a). Then, LR MMW images are input to MDCNN network for training. Fig. 1(b) shows the test process. Untrained images are input into the trained MDCNN, and the reconstructed SR MMW images can be obtained. Importantly, the specific network structure of MDCNN is shown in
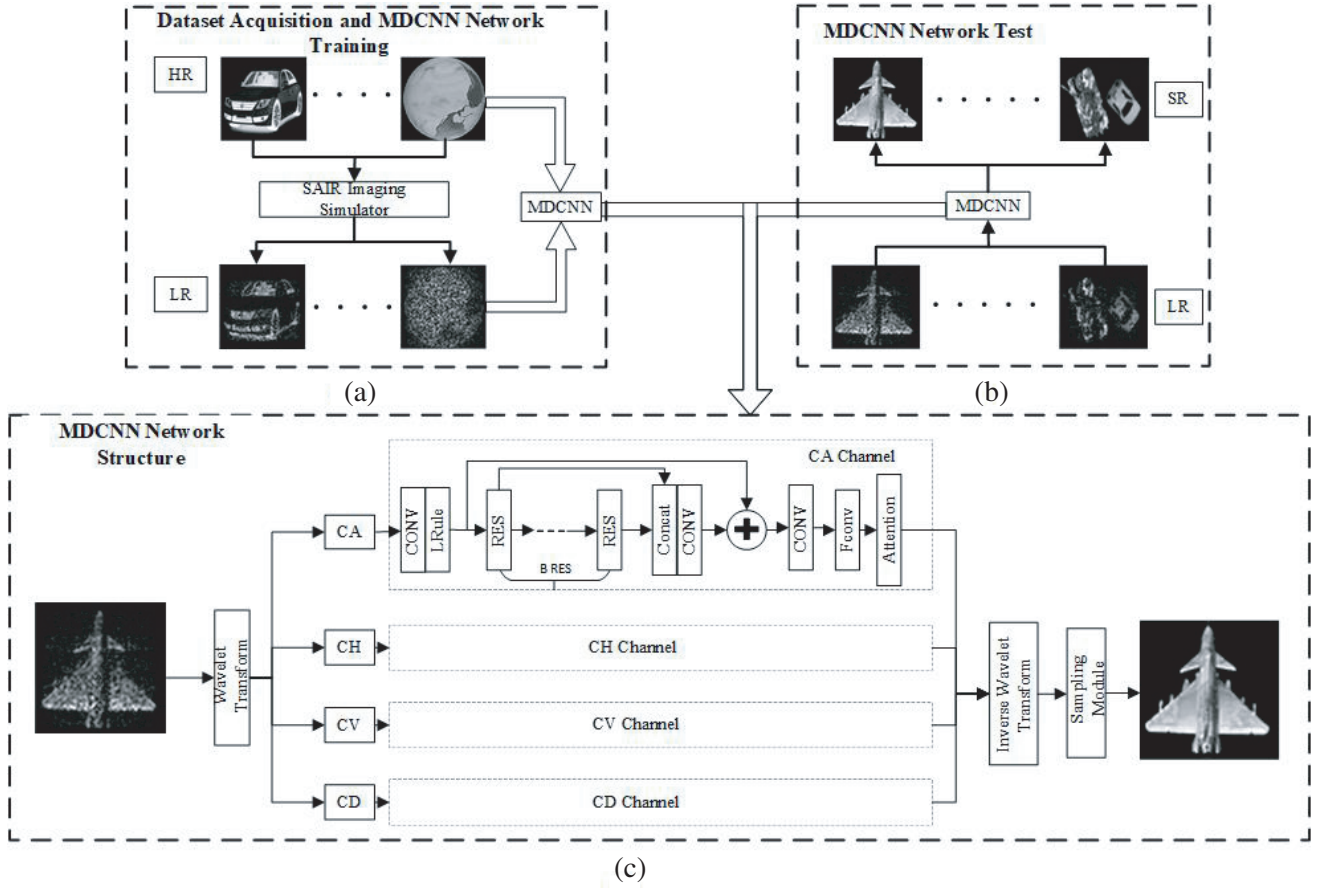
Figure 1. The structure diagram of MDCNN. (a) Data set acquisition and network training process. (b) Network test process. (c) MDCNN network structure.

Fig. 1(c). The multichannel model, wavelet transform, and residual block are combined to realize the enhancement of SAIR MMW image.

2.1. Data Set Acquisition and Training

In order to acquire a large data set, a SAIR imaging simulator is designed to obtain many MMW images. Since the imaging simulator completely simulates the real imaging process, the imaging principle of SAIR is only briefly described here.

As shown in Fig. 2, the antennas are located on plane OXY, and the extended radiation source S is located on plane oxy, whose brightness temperature image is $T(x, y)$. The plane OXY is parallel to the plane oxy, and the distance between the two planes is R. The radiation source S is dispersed into N small parts. The distances between the n-th radiation source S_n and antennas c and l are R_n^c and R_n^l, respectively [13]. According to [16], the visibility function of the antenna can be expressed as:

$$V_{c_l} = \left\langle E_c\left(R_n^c, t\right) \cdot E_l^*\left(R_n^l, t\right) \right\rangle$$

$$= \sum_{n=0}^{N} T(n) F_c\left(x_n, y_n\right) F_l^*\left(x_n, y_n\right) e^{-jk\left(R_n^c - R_n^l\right)} \tag{1}$$

where $E_\#(t)$ is the scene radiation signal received by antenna#, (x_n, y_n) the coordinate of the n-th point radiation source, T the normalized brightness temperature, $F_\#$ the normalized antenna pattern of antenna#, and the index part is the most critical wave path difference in synthetic aperture imaging.
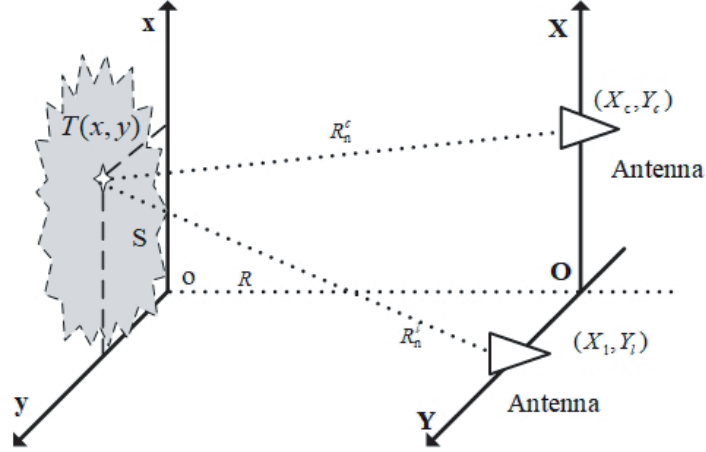
Figure 2. Geometry diagram of synthetic aperture imaging.

According to the geometric relationship diagram shown in Fig. 2, the exact expressions of the distances R_n^c and R_n^l can be expressed as:

$$R_n^c = \sqrt[2]{(x_n - X_c)^2 + (y_n - Y_c)^2 + R^2} \tag{2}$$

$$R_n^l = \sqrt[2]{(x_n - X_l)^2 + (y_n - Y_l)^2 + R^2} \tag{3}$$

Substituting Equation (2) and Equation (3) into Equation (1) directly, we can get the accurate visibility function.

$$
\begin{aligned}
V_{c_l} &= \left\langle E_c \left(R_n^c, t \right) \cdot E_l^* \left(R_n^l, t \right) \right\rangle \\
&= \sum_{n=0}^{N} T(n) F_c \left(x_n, y_n \right) F_l^* \left(x_n, y_n \right) e^{-jk\left[\left(\sqrt[2]{(x_n-X_c)^2+(y_n-Y_c)^2+R^2} - \sqrt[2]{(x_n-X_l)^2+(y_n-Y_l)^2+R^2} \right)\right]}
\end{aligned}
\tag{4}
$$

Rewrite Equation (4) into matrix form as:

$$V_{M\times 1} = G_{M\times N} T_{N\times 1} \tag{5}$$

where V is the vector form of visibility matrix, T the vector form of bright temperature image to be solved, and G the imaging matrix. The G-matrix can be obtained:

$$G(m,n) = F_c \left(x_n, y_n \right) F_l^* \left(x_n, y_n \right) e^{-jk\left[\left(\sqrt[2]{(x_n-X_{ml})^2+(y_n-Y_{ml})^2+R^2} - \sqrt[2]{(x_n-X_{mc})^2+(y_n-Y_{mc})^2+R^2} \right)\right]} \tag{6}$$

(X_{mc}, Y_{mc}) and (X_{ml}, Y_{ml}) are the coordinates of antennas c and l.

The MMW image can be reconstructed by solving the inverse process of Equation (5). The regularization method is used to solve the inverse process, and the solution model can be written as follows [17–19]:

$$\min_T E(T) = \parallel GT - V \parallel_2^2 + \alpha P(T) \tag{7}$$

where $\parallel GT - V \parallel_2^2$ is the fidelity term (data fitting term), ensuring that the difference between the original visibility function and the visibility function corresponding to the final solution is small enough. $P(T)$ is the regularization term (constraint condition), and α is the regularization parameter, which is used to balance the fidelity term and the regularization term.

In this paper, the data set is acquired by SAIR simulator which models the above imaging process. The specific process is shown in Fig. 1(a). More descriptions of data set acquisition process are presented as follows.

(1) More than 10800 natural images with a single target are selected from multiple databases as the input image for the SAIR simulator.

(2) All images are adjusted to 100×100 pixels. The preprocessed HR images are input to SAIR simulator. By simulating the imaging process of the actual integrated imaging radiometer, the SAIR simulator generates the corresponding LR MMW images.

(3) The preprocessed HR images and LR MMW images constitute HR-LR image data sets with one-to-one correspondence, which are sent to MDCNN network for training.

The specific details of SAIR imaging simulator will be described in Section 3.1.

2.2. Multi-Channel Depth Convolution Neural Network

Due to the use of aperture synthesis technology, it is difficult for SAIR to receive all the radiation. The loss of some signals leads to the low sensitivity of SAIR. In addition, because of the influence of near-field spherical wave and the interference of observation noise, the quality of the LR MMW image is poor. In order to process the LR MMW image more pertinently, MDCNN based on deep learning is proposed to achieve SR of the LR MMW image. Since the high and low frequency components of image store different image information, the wavelet transform is embedded into the network to obtain the high and low frequency components of image. The LR MMW image is divided into four independent components in this way. According to the different features of the four image components, different residual blocks are placed on the corresponding channels for feature extraction. Considering the different positions of the same feature channel and the importance of different feature channels, the channel attention mechanism is embedded in each channel. In addition, the network structure and layers are reasonably set, which can improve the utilization of high-frequency information, denoise low-frequency information, and improve the feature extraction ability of the network.

The specific structure of MDCNN is shown in Fig. 1(c). Firstly, four image components are obtained by wavelet transform of the LR MMW image. Each component is input to the corresponding independent component channel for feature extraction. In channel, each image component firstly passes through a shallow convolution layer to extract shallow features and then enters the corresponding dense residual module to extract deep features. The residual structure of each channel is shown in Fig. 4 to Fig. 6. The results of each residual block will be input into the global fusion layer to realize feature fusion. After that, a 1×1 convolution layer is set to reduce the amount of data fusion results. Then, the shallow features and deep features are added to make full use of all effective information. In addition, because deconvolution can maximize the recovery of the missing information, the obtained feature extraction results are input into the deconvolution layer for feature recovery. After that, the attention mechanism module receives the deconvolution result and automatically calculates the weight of the result to obtain the most important features required by the subsequent inverse wavelet transform. The attention mechanism module mainly uses the interdependence between features to retain key features and reduce the proportion of unnecessary features in the training process. This paper adopts the Convolutional Block Attention Module (CBAM) with good mobility [14]. The module includes two parts. It pays attention to not only the layer-to-layer feedback between the channels but also the feedback in the spatial dimension. It can be embedded in many mainstream networks and can improve the feature extraction ability of the network model without significantly increasing the amount of calculation and parameters. In this paper, CBAM is embedded in front of the wavelet inverse transform, which can automatically calculate the proportion of each channel according to effectiveness. Finally, SR MMW image is obtained by inverse wavelet transform.

2.2.1. Wavelet Transform

Wavelet transform is a multi-scale and multi-resolution decomposition tool. It can realize distortion-free frequency domain division, which helps to obtain the frequency domain components of different features of MMW image [15]. The wavelet transform is realized by 2D convolution.

Figure 3 shows the basic process of the 2D discrete wavelet transform. In the process of frequency separation, the image X passes through a low-pass filter and a high-pass filter firstly, and then half down-sampled along columns to obtain the low-frequency component L and high-frequency component H in the horizontal direction. After that, two components are transmitted to low-pass and high-pass filters, respectively, and further half down-sampled along rows. Finally, the outputs are four components, denoted as A, V, H, and D, which comprise average, vertical, horizontal, and diagonal information
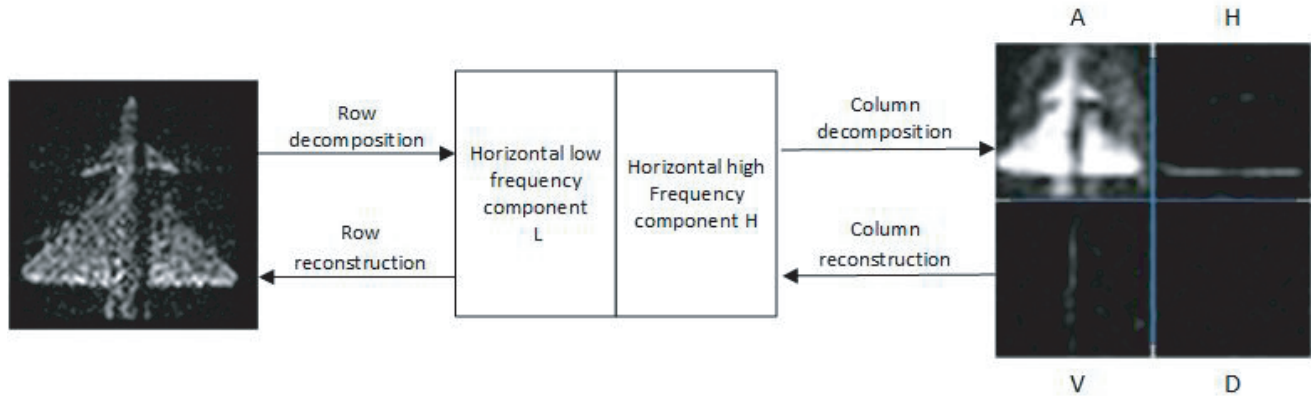
Figure 3. Schematic diagram of wavelet transform.

details from the original image. In addition, each sub-band is half the size of X. In wavelet transform, all transform kernels are "Haar" core.

The reconstruction process is the inverse of the decomposition process. Firstly, each column of the transformation result is inversely transformed, then each row is inversely transformed to obtain the reconstructed image. This way will not lose effective information, but also reduce the difficulty of feature extraction. Meanwhile, it can make full use of effective features. As shown in Fig. 3, the input X will be decomposed into four components. It can be seen from the image that component A contains most of the contour information of the X, with more noise. Component H and component V are mainly the texture information in the horizontal and vertical directions, with some effective information and a small amount of noise. The texture information of component D is not obvious, and the noise and effective information are difficult to distinguish.

With the help of wavelet transform, MDCNN learns and predicts four channels. Since different image details are retained in four channels rather than in a large image, the learning difficulty of the network can be significantly reduced.

2.2.2. Residual Block

After the processing of the wavelet transform module, the MMW image is explicitly divided into four components. According to the different characteristics of the four independent components, a more targeted network is established to further improve the effect of SR network. The low-frequency component of MMW image has abundant information, but contains more noise which leads to low readability of MMW image. Therefore, the feature extraction module of low-frequency channel needs more complex structure. The vertical and horizontal high-frequency channels are mainly the detailed texture information. There are a little effective information, but it is easy to distinguish from noise, and the feature extraction module with low complexity is designed. Since diagonal component information is little, we must extract it from the network with high complexity to use this information. In this paper, three residual blocks with different complexities are designed. According to the characteristics of each channel, they are placed in four channels to improve the feature extraction ability of the network.

The structure of the residual block of channel A is shown in Fig. 4. The residual block adopts a shallow structure. It is composed of two convolution layers and an identity map. The activation function is added after each convolution layer. Because there are negative numbers in the data obtained by wavelet transform, Leaky ReLU function is used as the activation function after all convolution layers. The convolution results of each layer are added with the original data F_0 to fully extract the effective features.

Figure 5 shows the residual block of H and V channels. Due to the H and V components having similar characteristics, the same channel structure is adopted. Effective information and noise are little, so the residual structure adopts single-layer convolution layer and identity mapping. The convoluted data F_c is added to the original data F_0.

Figure 6 shows the residual block of D channel. The D component also belongs to the high-
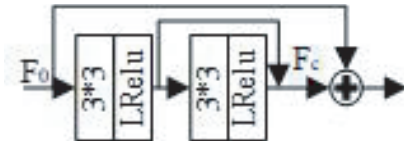
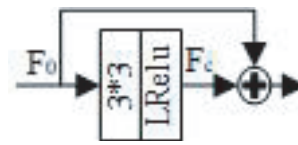**Figure 4.** The residual block of Channel A.

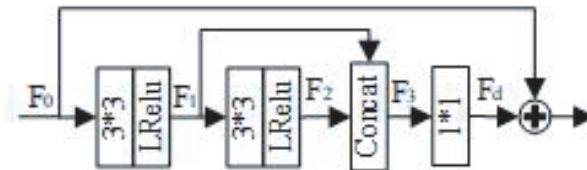**Figure 5.** The residual block of Channel V and H.

Figure 6. The residual block of Channel D.

frequency part of the image, which mainly contains the diagonal texture detail information and has the least effective data. Therefore, the residual structure is composed of multi-layer convolution layers and identity mapping. The data F_0 passes through a convolution layer, and the results are input to the fusion layer for local feature fusion. After that, the amount of data is reduced through a 1×1 convolution layer, and the convoluted data F_d is added with the original data F_0.

3. SIMULATION AND RESULTS

3.1. Data Set Acquisition and Training

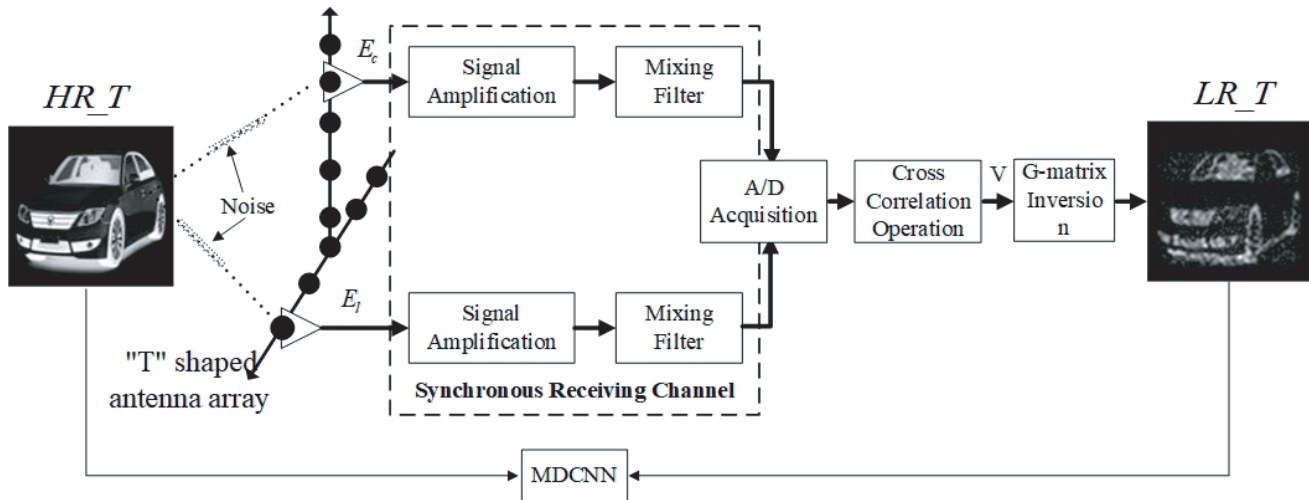The structure of SAIR simulator is shown in Fig. 7.

**Figure 7.** The structure of SAIR simulator.

Firstly, the "T" shaped antenna array collects the MMW radiation signal of the target scenario (image HR_T), and the signals E_c and E_l are obtained by integrating the MMW radiation signal. After amplifying, mixing, and sampling, the weak E_c and E_l signals are input to the data processing unit, where the visibility function V is obtained by complex correlation operation. Then the LR MMW image (LR_T) is obtained by solving Equation (7). Finally, HR_T and LR_T are transmitted to MDCNN for training as data set. In the simulation process, the gray value of the HR image is used as the radiation

Table 1. Parameter settings of the imaging simulator.

Parameter	Wavelength	Antenna aperture	Array size	Imaging distance	Antenna spacing	System resolution	Source spacing
Values	3 mm	0.5 m	50 * 50	6 m	1 cm	3.2 cm	1.6 cm

intensity of the radiation source, and the radiation source spacing is set to half of the system resolution. The parameter settings of the SAIR imaging simulator are shown in Table 1.

The MDCNN training process is shown in Fig. 8. 10700 LR MMW images are selected as the input of the MDCNN network, and the SR MMW images are used as the output of the MDCNN network. The weights of feature extraction module in independent component channels are updated by calculating the loss functions of SR MMW images and HR natural images. Then the SR MMW images closer to HR images can be reconstructed directly from LR images through the trained MDCNN. The specific parameter settings of MDCNN training are shown in Table 2.
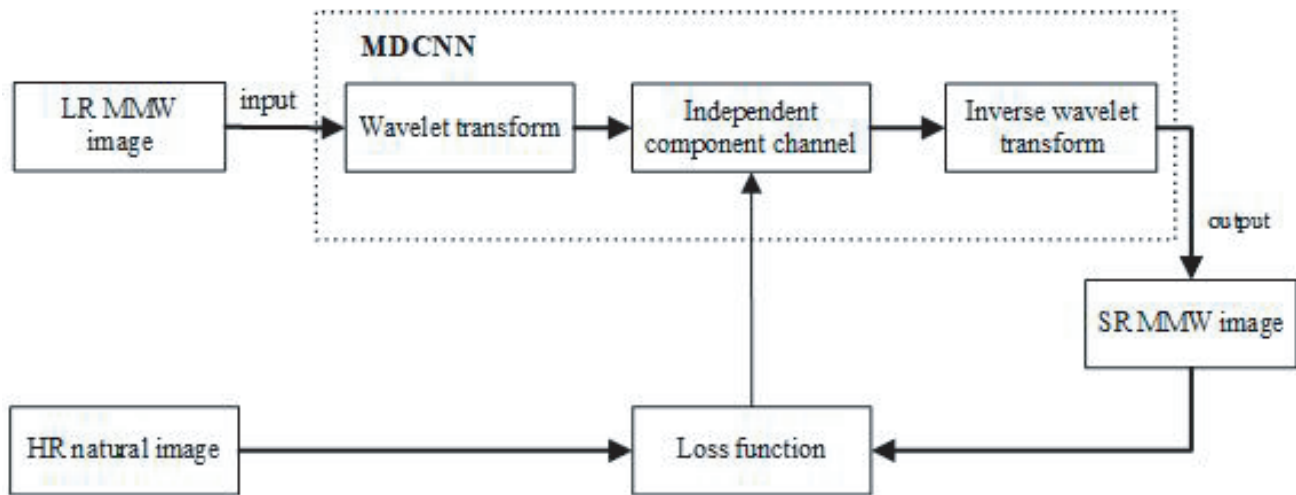
Figure 8. Flow chart of MDCNN training process.

Table 2. Parameter settings of the MDCNN.

Parameter	Batch size	Epoch	Patch size	channel width	Initial learning rate	Adam	leaky ReLU	Number of residual blocks
Values	64	1000	50 * 50	64	$\lambda = 0.01$	$\beta1 = 0.9,$ $\beta2 = 0.999$	$\alpha = 0.1$	$L = 9$

Peak signal-to-noise ratio (PSNR) and structural similarity index (SSIM) are used to measure the quality of SR in this paper. The higher the PSNR value is, the higher the similarity is between SR image and HR image, and the better the network performance is. SSIM ranges from 0 to 1, and the higher the value is, the higher the structural similarity is between the two images. In addition, the loss function adopts L1 loss function, which has better performance than other loss functions in terms of PSNR and SSIM. The gradient of weight and deviation is obtained by using the value of loss function, and the weight and deviation are attenuated. Adaptive learning rate is used for training. After about

1000 times of training sessions, the error between the HR image and the SR image is reduced to a relatively small value. All networks are in Python 3.7 and use GPU (NVIDIA geforcertx2080ti) to train on the workstation.

3.2. Analysis of Test Results

The network test process is shown in Fig. 1(b), and the LR MMW image is used as input and the reconstructed SR image used as output. We select 100 untrained images as the test set to test the network performance. In order to verify the effectiveness of the proposed SR network, two kinds of simulation experiments are carried out in this paper. We compared it with SRCNN, RDN, and THZ algorithms. The residual block of all networks is set to 9 and the same data set is used to more accurately reflect the advantages and disadvantages of the network. In order to objectively evaluate the accuracy of the SR results, PSNR and SSIM of the test set are calculated, and the results are shown in Table 3.

Table 3. Comparison of average PSNR and SSIM of test set.

Evaluation	LR MMW image	SRCNN	RDN	THZ	MDCNN
PSNR	15.2597	16.4853	17.0327	17.0695	17.5835
SSIM	0.1532	0.1530	0.2225	0.1748	0.2533

The data shows that the quality of the MMW image generated by SR network is better than the original LR MMW image. Among them, MDCNN has the highest PSNR and SSIM, which also proves the advantage of MDCNN in improving the MMW image quality.

In order to reflect the characteristics of MMW suitable for metal detection, the tank&car and airplane are selected as simulated test images for qualitative analysis. The HR images input in SAIR simulator are shown in the Fig. 9(a) and Fig. 10(a). The LR MMW images generated by SAIR simulator are shown Fig. 9(b) and Fig. 10(b). In order to prove the effectiveness of the proposed SR network, we compare it with the results of SRCNN, RDN, and THZ algorithms. The results are shown in Figs. 9(c) ∼ (f) and Figs. 10(c) ∼ (f).
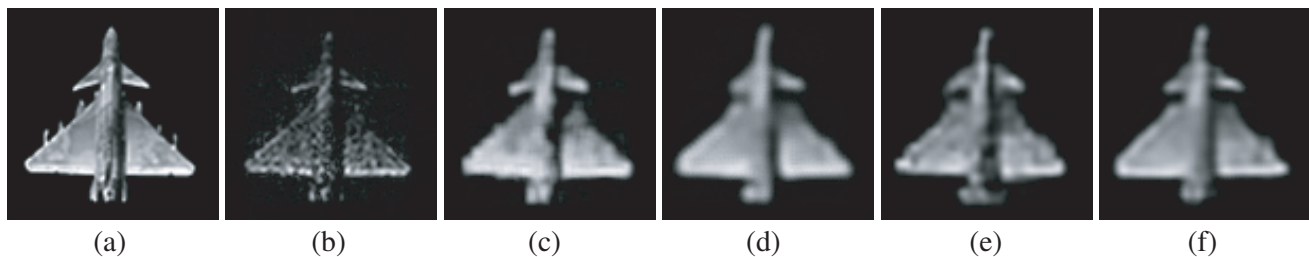

(a) (b) (c) (d) (e) (f)

Figure 9. The reconstructed images of airplane Scene. (a) HR. (b) LR MMW image. (c) SRCNN. (d) THZ. (e) RDN. (f) MDCNN.

From Fig. 9(b) and Fig. 10(b), it can be found that the LR MMW image has poor quality and a lot of noise. Moreover, the outline is not clear, and it is difficult to identify the object category. It can be seen from Figs. 9(c) ∼ (f) and Figs. 10(c) ∼ (f) that the image quality is significantly enhanced; the contour is clear; and most of the noise is removed after SR. Meanwhile, these pictures also show the advantages and disadvantages of four neural networks for MMW image processing. The images reconstructed by SRCNN are fuzzy with more noise inside, and the image contour is not obvious. Compared with SRCNN, the reconstruction effect of THZ is improved to some extent, but the internal effective information is removed while removing noise. The image results of RDN have high accuracy. It removes most of noise and restores the target information effectively. The proposed MDCNN pays more attention to the information of each component and simplifies the complexity of the model by
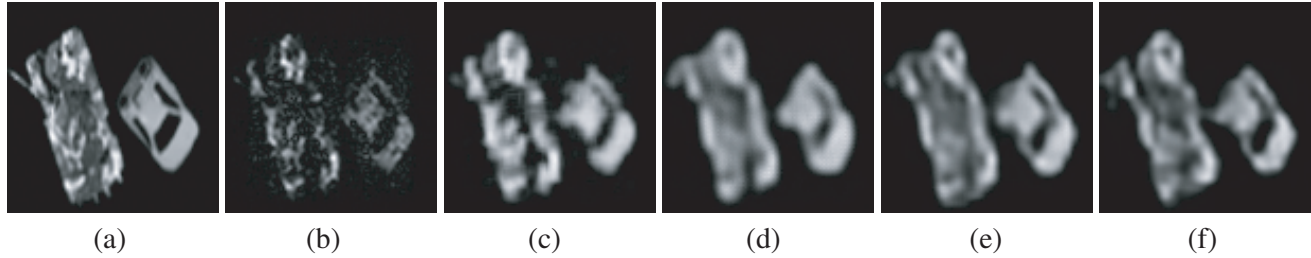
| (a) | (b) | (c) | (d) | (e) | (f) |

Figure 10. The reconstructed images of the tank&car. (a) HR. (b) LR MMW image. (c) SRCNN. (d) THZ. (e) RDN. (f) MDCNN.

extending the network. It not only removes most of the noise, but also retains many effective features inside the image, making the contour and details of the reconstructed image clearer and recognizable. The MDCNN successfully reconstructs the detail texture and edge in SR image, achieving better SR output than other models.

For more accurate proof, we calculated the PSNR and SSIM values of tank&car and airplane images. The results are shown in Table 4. It can also be seen from the data that for these images, the image quality processed by the neural network is good. Among them, MDCNN achieves the largest PSNR and SSIM.

Table 4. Comparison of PSNR and SSIM of tank&car and airplane image.

Scence	Evaluation	LR MMW image	SRCNN	RDN	THZ	MDCNN
airplane	PSNR	13.7016	15.6145	19.7470	19.6656	20.0230
	SSIM	0.1138	0.2068	0.4720	0.4468	0.6065
tank&car	PSNR	16.6457	18.2867	19.7934	19.6648	19.8889
	SSIM	0.2017	0.4647	0.5344	0.6042	0.6279

4. CONCLUSION

In this paper, to improve passive near-field MMW image quality effectively, we propose a convolutional neural network named MDCNN. The LR MMW image is obtained through the SAIR imaging simulator. With the help of multichannel model, wavelet transform, and dense residual technology, high frequency and low frequency components of LR MMW images are extracted in MDCNN, and then transmitted to more targeted residual structures to denoise and enhance the target information in four independent channels, respectively. The experimental results show that MDCNN is superior to other SR methods in visual effect and higher than other SR models in PSNR and SSIM.

REFERENCES

1. Clark, S. E., J. A. Lovberg, C. A. Martin, and V. G. Kolinko, "Passive millimeter-wave imaging for airborne and security applications," *Passive Millimeter-Wave Imaging Technology VI and Radar Sensor Technology VII*, 16-21, International Society for Optics and Photonics, 2003.
2. Camps, A., J. Bará, I. C. Sanahuja, and F. Torres, "The processing of hexagonally sampled signals with standard rectangular techniques: Application to 2-d large aperture synthesis interferometric radiometers," *IEEE Transactions on Geoscience and Remote Sensing*, Vol. 35, No. 1, 183–190, 1997.

3. Duffo, N., I. Corbella, F. Torres, A. Camps, and M. Vall-llossera, "Advantages and drawbacks of near field characterization of large aperture synthesis radiometers," *8th Specialist Meeting on Microwave Radiometry and Remote Sensing Applications*, 24–27, University La Sapienza, Rome, 2004.

4. Chen, J., Y. Li, J. Wang, Y. Li, and Y. Zhang, "An accurate imaging algorithm for millimeter wave synthetic aperture imaging radiometer in near-field," Vol. 141, 517–535, 2013.

5. Van Ouwerkerk, J., "Image super-resolution survey," *Image and Vision Computing*, Vol. 24, No. 10, 1039–1052, 2006.

6. Zhou, F., W. Yang, and Q. Liao, "Interpolation-based image super-resolution using multisurface fitting," *IEEE Transactions on Image Processing*, Vol. 21, No. 7, 3312–3318, 2012.

7. Dong, C., C. C. Loy, K. He, and X. Tang, "Learning a deep convolutional network for image super-resolution," *European Conference on Computer Vision*, 184–199, Springer, 2014.

8. Dong, C., C. C. Loy, and X. Tang, "Accelerating the super-resolution convolutional neural network," *European Conference on Computer Vision*, 391–407, Springer, 2016.

9. Kim, J., J. K. Lee, and K. M. Lee, "Accurate image super-resolution using very deep convolutional networks," *Proceedings of the IEEE Conference on Computer Vision and Pattern Recognition*, 1646–1654, 2016.

10. Lim, B., S. Son, H. Kim, S. Nah, and K. Mu Lee, "Enhanced deep residual networks for single image super-resolution," *Proceedings of the IEEE Conference on Computer Vision and Pattern Recognition Workshops*, 136–144, 2017.

11. Zhang, Y., Y. Tian, Y. Kong, B. Zhong, and Y. Fu, "Residual dense network for image super-resolution," IEEE, 2018.

12. Long, Z., T. Wang, C. You, Z. Yang, K. Wang, and J. Liu, "Terahertz image super-resolution based on a deep convolutional neural network," *Applied Optics*, Vol. 58, No. 10, 2731–2735, 2019.

13. Chen, J., S. Zhang, and X. Zhu, "Higher-order moving target detection for rotating scanning synthetic aperture interferometric radiometer," *Progress In Electromagnetics Research Letters*, Vol. 82, 41–49, 2019.

14. Woo, S., J. Park, J.-Y. Lee, and I. S. Kweon, "CBAM: Convolutional block attention module," *Proceedings of the European Conference on Computer Vision (ECCV)*, 3–19, 2018.

15. Shin, D. K. and Y. S. Moon, "Super-resolution image reconstruction using wavelet based patch and discrete wavelet transform," *Journal of Signal Processing Systems*, Vol. 81, No. 1, 71–81, 2015.

16. Tanner, A., B. Lambrigsten, T. Gaier, and F. Torres, "Near field characterization of the geostar demonstrator," *2006 IEEE International Symposium on Geoscience and Remote Sensing*, 2529–2532, IEEE, 2006.

17. Lannes, A., É. Anterrieu, and K. Bouyoucef, "Fourier interpolation and reconstruction via shannon-type techniques: I. Regularization principle," *Journal of Modern Optics*, Vol. 41, No. 8, 1537–1574, 1994.

18. Lannes, A., É. Anterrieu, and K. Bouyoucef, "Fourier interpolation and reconstruction via shannon-type techniques II. Technical developments and applications," *Journal of Modern Optics*, Vol. 43, No. 1, 105–138, 1996.

19. Lewis, B. and F. Sgallari, "Tikhonov regularization with nonnegativity constraint," *Electronic Transactions on Numerical Analysis*, Vol. 18, 153–173, 2004.